UC Santa Cruz
UC Santa Cruz Previously Published Works

Title

Imaging ruptured lithosphere beneath the Red Sea and Arabian Peninsula

Permalink

https://escholarship.org/uc/item/4ps1684s

Journal

Earth and Planetary Science Letters, 259

Authors

Hansen, Samantha E.
Rodgers, Arthur J.
Schwartz, Susan Y.
et al.

Publication Date

2007-07-01

Peer reviewed

1   **Imaging Ruptured Lithosphere Beneath the Red Sea and Arabian Peninsula**

2   Samantha E. Hansen[a,b] (shansen@es.ucsc.edu), Arthur J. Rodgers[b] (rodgers7@llnl.gov), Susan

3   Y. Schwartz[a] (susan@es.ucsc.edu), and Abdullah M.S. Al-Amri[c] (amsamri@ksu.edu.sa)

4   [a]Earth and Planetary Sciences Department, University of California, Santa Cruz

5   1156 High St., Santa Cruz, CA, 95064, USA

6   [b]Energy and Environment Directorate, Lawrence Livermore National Laboratory

7   7000 East Ave., Livermore, CA, 94551, USA

8   [c]Geology Department and Seismic Studies Center, King Saud University

9   P.O. Box 2455, Riyadh, 11451, Saudi Arabia

10   Corresponding Author: Samantha E. Hansen

11   (831) 459-4426 (tel)

12   (831) 459-3074 (fax)

13   shansen@es.ucsc.edu

14   **Abstract**

15   The Red Sea Rift, an archetype of a newly formed ocean basin, is an ideal environment in

16   which to study the controversial processes associated with continental rifting. Different models

17   have been proposed to explain how rifting in the Red Sea evolved; however, accurate constraints

18   on lithospheric structure have not been available to discriminate rifting models. We use the S-

19   wave receiver function technique to produce the first images of the lithosphere-asthenosphere

20   boundary (LAB) structure along the Red Sea and throughout the Arabian Peninsula.

21   Lithospheric thickness varies considerably, with thin lithosphere centered on the rift axis,

22   thickening toward the Arabian interior. Gravity data are well fit by our structural model and

23   indicate that high surface topography along the rift flank is not in isostatic equilibrium, requiring

24   dynamic compensation for its support. While our derived structure is consistent with active

25   rifting processes, previous studies demonstrated that the Red Sea initiated as a passive rift.

26   Therefore, our results suggest a two-stage rifting history, where extension and erosion by flow in

27   the underlying asthenosphere are responsible for variations in LAB depth. LAB topography

28   guides asthenospheric flow beneath western Arabia and the Red Sea, demonstrating the

29   important role lithospheric variations play in the thermal modification of tectonic environments.

30   **Keywords:** Arabia, Red Sea, rifting, lithosphere-asthenosphere boundary, S-receiver functions

31   **1. Introduction**

32   Rifting of the Red Sea began about 30 million years ago, separating the western edge of

33   the Arabian Plate from Africa [1]. Some studies [2-4] suggest that the Red Sea developed as a

34   passive rift, where extensional stresses due to far-field body forces are accommodated on low-

35   angle detachment planes extending through the entire lithosphere below the rift (Fig. 1a). This

36   results in passive upwelling of asthenospheric material below the rift and asymmetric thinning,

37   where the thinnest lithosphere is laterally offset from the rift axis. Other studies [5-6] argue that

38   the Red Sea is an active rift, where the lithosphere is thermally eroded by flow in the underlying

39   asthenosphere, requiring the presence of hot, ascending material (Fig. 1b). In this case, the rift

40   flanks are thermally uplifted, and the area of greatest lithospheric thinning is coincident with the

41   rift axis. It has also been suggested that these two end-member models are not mutually

42   exclusive; rifting in the Red Sea may have been initiated by passive processes, followed by more

43   recent active processes associated with a mantle upwelling [1, 7-8].

44   The Arabian Peninsula is composed of the western Arabian Shield and the eastern

45   Arabian Platform (Fig. 2). The Shield is composed of Proterozoic island arc terranes that were

46   accreted together 600-900 Ma, and basement rocks in this region have little to no sediment

47   cover. However, the Proterozoic basement rocks in the Platform are covered by up to 10 km of

48   Phanerozoic sediments [9]. Seismic body and surface wave tomography studies [10-14] have

49   shown that the upper mantle beneath the Arabian Shield and the Red Sea is anomalously slow,

50   most likely associated with a shallow lithosphere-asthenosphere boundary (LAB), and that

51   velocities increase towards the continental interior. Additionally, an abrupt change in the

52   lithospheric structure across the Shield-Platform boundary has been inferred [13-14]. Estimates

53   of lithospheric thickness from seismic refraction, P-wave receiver function (PRF), xenolith, and

54   isotope studies vary from about 40 km near the Red Sea coast to about 100 km in the Arabian

55   interior [1,15-17]. However, these studies do not provide accurate and spatially complete

56   estimates of lithospheric thickness to discriminate the type of rifting occurring in the Red Sea.

57   In this study, we use the S-wave receiver function (SRF) technique [18-21] to determine

58   the LAB depth by identifying S-to-P (Sp) conversions from discontinuities beneath seismic

59   stations, thereby providing a direct constraint on the lithospheric thickness and new insights into

60   the passive-active rifting debate. Unlike PRFs, where crustal multiples can mask the conversion

61   from the LAB, boundary conversions on SRFs can be more clearly identified because they arrive

62   earlier than the direct S phase while all crustal multiples arrive later. We demonstrate that the

63   lithospheric thickness varies considerably beneath Arabia, with the thinnest lithosphere centered

64   on the Red Sea Rift axis. Our structural model is consistent with gravity data collected by the

65   GRACE satellites [22] and, in conjunction with previous findings, suggests a two-stage rifting

66   history, where extension and erosion by flow in the asthenosphere are responsible for variations

67   in LAB topography.

68   **2. Data and Methodology**

3

69   Teleseismic waveform data recorded by broadband instruments from four different

70 seismic networks were used. The largest array, the Saudi Arabian National Digital Seismic

71 Network (SANDSN), includes 27 broadband stations distributed along the eastern edge of the

72 Red Sea and across the Arabian Peninsula [23] (Fig. 2, Table 1). SANDSN data from events

73 occurring since 2000 were used for this study. To supplement the SANDSN coverage, we also

74 analyzed data recorded by the eight IRIS-PASSCAL Saudi Arabian Broadband Array stations,

75 which operated from November 1995 to March 1997 [24], data from two stations deployed in

76 Jordan, which operated between 1998 and 2001 [25], and data recorded by two stations in the

77 UAE from 2003 and 2004 [26] (Fig. 2, Table 1).

78   In general, the receiver function method utilizes coordinate rotation and deconvolution to

79 identify converted phases from seismic discontinuities. To detect Sp conversions, three-

80 component seismic data must be rotated around the incidence angle into the SH-SV-P coordinate

81 system [19]. This rotation is critical because if an incorrect incidence angle is used, noise can be

82 significantly enhanced and major converted phases may become undetectable. In addition, since

83 S-waves have lower frequencies than P-waves, more restrictive event selection and different

84 filtering limits are required for SRF analysis as compared to PRF analysis [18-21].

85   We selected S-waves with high signal-to-noise ratios from earthquakes with magnitudes

86 larger than 5.7 in a distance range of 60° to 85°. Waveforms were first rotated from the N-E-Z to

87 the R-T-Z coordinate system using the event's back-azimuth and were visually inspected to pick

88 the S-wave onset. The three-component records were then cut to focus on the section of the

89 waveform that is 100 s prior to the S arrival and 20 s after. To rotate the data into the SH-SV-P

90 coordinate system, a subroutine was developed, based on the approach of Sodoudi [27], to

91 determine the correct incidence angle. The cut R-T-Z seismograms were rotated through a series

92   of incidence angles to create a set of quasi-SV and quasi-P data. Each quasi-SV component is

93   then deconvolved from the corresponding quasi-P component using Ligorria and Ammon's

94   iterative time domain method [28], which creates a SRF. To make the SRFs directly comparable

95   to PRFs, both the time axes and the amplitudes of the SRFs are reversed [18-21]. The frequency

96   content of the receiver function is controlled by the Gaussian width factor, a [28]. For PRF

97   analysis, common values of a are about 2.5; however, a smaller a of 1.0 was used for the lower

98   frequency SRF analysis.

99   To limit our examination to the true P, SV components and their corresponding receiver

100   function, we found the incidence angle that minimizes the direct S-wave energy on the P-

101   component. On the time-reversed receiver functions, the direct S arrival is at 0 s. Therefore, we

102   are only interested in the receiver function whose mean amplitude is closest to zero at zero time.

103   A second algorithm was developed to examine all the generated receiver functions for a given

104   event and determine which record best meets this criterion. The P, SV components and the

105   corresponding receiver function with the appropriate incidence angle are retained, and the

106   remaining records are discarded.

107   Once receiver functions were generated for all events at an examined station, a move-out

108   correction was applied to the receiver functions to correct for variations in distance between

109   events. Again, to make the SRFs directly comparable to PRFs, we used a reference P-wave

110   slowness of 6.4 s/deg [18-21, 27]. Each individual receiver function was then visually inspected

111   and compared to previously determined PRFs [17, 29] at the same station to identify the crust-

112   mantle boundary (Moho) conversion. Only SRFs that display a clear Moho conversion at the

113   appropriate time were used for further analysis. These records were then stacked to enhance the

114   LAB conversion (Fig. 3). Stacked SRFs were generated for 29 of the 39 total stations. For the

115 remaining stations, stacks could not be created due to either a lack of data or poor signal-to-noise

116 ratios (Table 1).

117 *2.1. Synthetic SRFs*

118 The SRF stacks were modeled using synthetic receiver functions generated by the

119 reflectivity method [30]. Using published S-wave velocities (V_S) [17, 31], simple one

120 dimensional models were constructed to match the amplitude and timing of both the Moho and

121 LAB conversions, providing constraints on the velocity contrast and the depths of these

122 boundaries, respectively (Fig. 3, Table 1). On average, the crustal and upper mantle V_S needed

123 to fit the Moho amplitude were about 3.6 and 4.5 km/s, respectively. These are similar to the V_S

124 used to fit the Moho amplitude on the SANDSN PRFs [29]. To fit the LAB amplitude, an

125 average lower mantle V_S of about 4.2 km/s was required. In all cases, a default Poisson's ratio

126 (σ) of 0.25 was used.

127 It should be noted that the average V_S and default σ used to generate the synthetics differ

128 from those found by waveform modeling. Rodgers et al. [31] reported average crustal V_S of 3.7

129 and 3.5 km/s and average upper mantle V_S of 4.3 and 4.55 km/s for the Arabian Shield and

130 Platform, respectively. In addition, the reported σ in the Arabian Shield mantle was 0.29 while

131 in the Platform it was 0.27. Testing revealed that the waveform modeling velocities did not fit

132 the SRF amplitudes as well, but the timing of the phases only changed by a few tenths of a

133 second. Therefore, the difference in V_S only leads to about a 3-5 km difference in depth.

134 However, the timing of the phase conversions is more dependent on σ, where larger values, such

135 as those suggested by the waveform modeling, result in earlier arrivals and shallower

136 discontinuity depths. Based on the amount of variation observed for different values of V_S and

137 σ, the estimated errors for the reported Moho and LAB depths are 5 and 10 km, respectively.

138   **3. Results**

139   Generally, both the Moho and LAB are shallowest near the Red Sea and become deeper

140   towards the Arabian interior (Fig. 4). Given the configuration of stations, the boundary depths

141   along profile AA' (Fig. 4) are highlighted to examine the structure beneath both the Arabian

142   Shield and Platform. Also, since seafloor spreading is more developed in the southern Red Sea

143   [32], this profile provides a view of the most extensively rifted portion of the lithosphere.

144   However, for comparison, the structure along the more northern profile BB' (Fig. 4) is also

145   presented.

146   Near the coast, the Moho depth in southern Arabia increases from about 12 to 35 km,

147   with a few exceptions showing a deeper Moho beneath stations that are situated on higher

148   surface topography along the southern Red Sea coast in the Asir province (ex. stations NAMS,

149   SODA, and DJNS, Fig. 1). The crustal thickening along profile AA' continues until an average

150   Moho depth of about 40-45 km is reached beneath both the central Arabian Shield and Platform

151   (Fig. 4a). The LAB near the coast is at a depth of about 50 km; however, it rapidly deepens to

152   attain a maximum depth of about 120 km beneath the Arabian Shield within 300 km of the Red

153   Sea. At the Shield-Platform boundary, a step is observed in the lithospheric thickness where the

154   LAB depth increases to about 160 km (Fig. 4b).

155   Boundary depths along profile BB' are comparable to those at similar distances along

156   profile AA'. The Moho depth near the coast is about 22-25 km, and crustal thickening continues

157   until an average Moho depth of about 35-40 km is reach beneath the interior Arabian Shield (Fig.

158   4a). The LAB near the coast is at a depth of about 55 km; however it also deepens beneath the

159   Shield to attain a maximum depth of 100-110 km (Fig. 4b). The broad spatial coverage of these

7

160 estimates provides the first images of ruptured continental lithosphere on a scale applicable to

161 geodynamical modeling.

162 *3.1. Gravity Comparison*

163   The inferred lithospheric structure along both profiles is tested by comparing its predicted

164 gravity signature to data collected by the GRACE satellites [22]. Average seismic velocities

165 from both the current and previous studies [17, 31] were converted to density estimates using the

166 Nafe-Drake relationship [33] and sediment thickness was extracted from a global sediment

167 model [34]. Along profile AA', the small-scale (50-200 km) recorded gravity signature can be

168 matched very well by making minor adjustments to the Moho and LAB boundaries (well within

169 the estimated error). Broad-scale gravity observations require a shallow asthenosphere beneath

170 the Red Sea, with the thinnest lithosphere centered on the rift axis (Fig. 5).

171   Profile BB' is shorter, has fewer stations and therefore fewer constraints, so we set the

172 lithospheric thickness beneath the rift axis to be similar to that on profile AA'. We then

173 examined if the calculated gravity signature is consistent with the recorded data. Small-scale

174 recorded gravity observations can again be matched very well by slightly adjusting the Moho and

175 LAB boundaries. Broad-scale gravity observations are also well fit by a shallow asthenosphere

176 beneath the Red Sea (Fig. 6). These findings demonstrate that the Moho and LAB SRF results

177 are consistent with gravity measurements across Arabia and support current active rifting

178 processes (Fig. 1b).

179 **4. Discussion and Conclusions**

180   The average elevation across Arabia is about 1 km; however, near the Red Sea, the

181 elevation is significantly higher, up to 3 km [8]. This high topography is not in isostatic

182 equilibrium with our lithospheric model resulting from the SRF analysis, requiring another

183   compensation mechanism. Potential mechanisms include flexural and dynamic compensation,

184   where the topography is supported by lithospheric rigidity or asthenospheric flow, respectively.

185   Using relationships that described the amplitude of deflection and degree of compensation for a

186   topographic load [35], we estimate that an elastic thickness of about 20 km is necessary to

187   support the rift flank. Analysis of the East African Rift indicates an elastic thickness less than 10

188   km [36]. If the elastic thickness of the Red Sea margin is comparable, flexure alone will not

189   support its topography and dynamic compensation must contribute to rift flank support.

190   Daradich et al. [8] computed mantle flow from seismic tomography and demonstrated that both

191   the rift flank topography and overall tilt of Arabia are dynamically supported.

192   Both the observed lithospheric thinning and the necessity for dynamic compensation

193   support active rifting processes. In the active rifting model (Fig. 1b), the rift event is preceded

194   by a period of uplift; however, in the passive rifting model (Fig. 1a), associated uplift postdates

195   the rifting event [4]. Geologic and fission track data show that western Arabia was at or below

196   sea level prior to 30 Ma and that the uplift of the Red Sea margin postdates the initiation of

197   rifting by about 5-10 million years [4]. These results demonstrate that the Red Sea began as a

198   passive rift [2-4]. The mantle temperature beneath the Arabian Shield, determined from

199   xenoliths, is abnormally high, but the surface heat flow is lower than global averages [4]. This

200   suggests that mantle temperatures have not had time to equilibrate at the surface. The thermal

201   disequilibrium, in conjunction with our SRF and gravity results, demonstrate that while active

202   rifting processes are currently affecting the Red Sea, these processes only developed within the

203   last 15-20 million years and therefore reflect a second stage of rifting. This may also explain

204   why the LAB in this region is such a sharp discontinuity. The presence of hot material beneath

205   Arabia associated with active upwelling could lead to some degree of partial melt, which would

9

206 significantly lower the asthenospheric shear velocity and result in a high velocity contrast across

207 the LAB. It has been suggested that the degree of partial melt beneath Arabia ranges between 4-

208 10% [1, 37].

209 Yuen and Fleitout [38] illustrated that the convection and heat associated with mantle

210 upwellings, in conjunction with extensional forces, can thin a 100-km-thick lithosphere at an

211 average rate of 7.5 km Myr^{-1}. Using this rate and approximating the starting lithospheric

212 thickness to be about 160 km (the thickness of the lithosphere at the Shield-Platform step), the

213 resulting, thinned lithosphere would have a thickness of about 50 km. This estimate agrees well

214 with our observed lithospheric thickness along the Red Sea coast and demonstrates that active

215 rifting forces could have generated the observed LAB topography over the last 15-20 Myr.

216 Therefore, our observations of lithospheric structure support a two-stage rifting history

217 along the Red Sea and suggest that the LAB topography is the result of extension and erosion

218 caused by asthenospheric flow. Previous studies [7-8] speculated at the existence of such

219 topography and suggested that it may direct asthenospheric flow beneath the Arabian Shield and

220 the Red Sea Rift. Inferred flow direction from shear-wave splitting results is also consistent with

221 this conclusion [39]. In addition, body and surface wave tomography [13-14] suggest that the

222 mantle lithosphere beneath the Arabian Shield has been thermally modified and that there is an

223 abrupt change in lithospheric structure across the Shield-Platform boundary. This structural

224 change is also observed in the gravity data (Fig. 5b), where the transition from the Shield to the

225 Platform is marked by a small-scale gravity anomaly. The LAB step imaged in this study may

226 reflect the pre-existing lithospheric thickness prior to the accretion of island arc terranes

227 composing the Arabian Shield. This step and the rapid lithospheric thinning near the rift likely

228   channelize hot asthenospheric flow as predicted [7-8, 39] and illustrate the important role

229   lithospheric variations play in the thermal modification of tectonic environments.

237   **References**

238   1. V. Camp, M. Roobol, Upwelling asthenosphere beneath western Arabia and its regional

239   implications, J. Geophys. Res. 97 (1992) 15255-15271.

240   2. B. Wernicke, Uniform-sense normal simple-shear of the continental lithosphere, Can. J.

241   Earth Sci. 22 (1985) 108-125.

242   3. W. Voggenreiter, H. Hötzl, A. Jado, Red Sea related history of extension and magmatism

243   in the Jizan area (southwest Saudi Arabia): Indication for simple-shear during Red Sea

244   rifting, Geol. Rund. 77 (1988) 257-274.

245   4. A. McGuire, R. Bohannon, Timing of Mantle Upwelling: Evidence for a Passive Origin

246   for the Red Sea Rift, J. Geophys. Res. 94 (1989) 1677-1682.

247   5. D. McKenzie, Some remarks on the development of sedimentary basins, Earth Planet.

248   Sci. Letts. 40 (1978) 25-32.

249   6. N. Bellahsen, C. Faccenna, F. Funiciello, J.M. Daniel, L. Jolivet, Why did Arabia

250   separate from Africa? Insights from 3-D laboratory experiments, Earth Plant. Sci. Letts.

251   216 (2003) 365-381.

252   7. C. Ebinger, N. Sleep, Cenozoic magmatism throughout east Africa resulting from impact

253   of a single plume, Nature 395 (1998) 788-791.

254   8. A. Daradich, J. Mitrovica, R. Pysklywec, S. Willett, A. Forte, Mantle flow, dynamic

255   topography, and rift-flank uplift of Arabia, Geology 31 (2003) 901-904.

256   9. D. Stoeser, V. Camp, Pan-African microplate accretion of the Arabian Shield, GSA Bull.

257   96 (1985) 817-826.

258   10. M. Benoit, A. Nyblade, J. VanDecar, H. Gurrola, Upper mantle P wave velocity structure

259   and transition zone thickness beneath the Arabian Shield, Geophys. Res. Letts. 30 (2003)

260   1-4.

261   11. E. Debayle, J. Leveque, M. Cara, Seismic evidence for a deeply rooted low-velocity

262   anomaly in the upper mantle beneath the northeastern Afro/Arabian continent, Earth

263   Planet. Sci. Letts. 193 (2001) 423-436.

264   12. J. Julia, C. Ammon, R. Herrmann, Lithospheric structure of the Arabian Shield from the

265   joint inversion of receiver functions and surface-wave group velocities, Tectonophysics

266   371 (2003) 1-21.

267   13. A. Nyblade, Y. Park, A. Rodgers, A. Al-Amri, Seismic Structure of the Arabian Shield

268   Lithosphere and Red Sea Margin, MARGINS newsletter 17 (2006) 13-15.

269   14. Y. Park, A. Nyblade, A. Rodgers, A. Al-Amri, Upper mantle structure beneath the

270   Arabian Peninsula from regional body wave tomography: Implications for the origin of

271   Cenozoic uplift and volcanism in the Arabian Shield, Geochem. Geophy. Geosy. in

272   review.

273   15. W. Mooney, M. Gettings, H. Blank, J. Healy, Saudi Arabian seismic refraction profile: A

274   traveltime interpretation of crustal and upper mantle structure, Tectonophysics 111

275   (1985) 173-246.

276   16. R. Altherr, F. Henjes-Kunst, H. Puchelt, A. Baumann, Volcanic activity in the Red Sea

277   axial trough – Evidence for a large mantle diapir, Tectonophysics 150 (1990) 121-133.

278   17. E. Sandvol, D. Seber, M. Barazangi, F. Vernon, R. Mellors, A. Al-Amri, Lithospheric

279   seismic velocity discontinuities beneath the Arabian Shield, Geophys. Res. Lett. 25

280   (1998) 2873-2876.

281   18. V. Farra, L. Vinnik, Upper mantle stratification by P and S receiver functions, Geophys.

282   J. Int. 141 (2000) 699-712.

283   19. X. Li, R. Kind, X. Yuan, I. Wolbern, W. Hanka, Rejuvenation of the lithosphere by the

284   Hawaiian plume, Nature 427 (2004) 827-829.

285   20. P. Kumar, R. Kind, W. Hanka, K. Wylegalla, C. Reigber, X. Yuan, I. Woelbern, P.

286   Schwintzer, K. Fleming, T. Dahl-Jensen, T. Larsen, J. Schweitzer, K. Priestley, O.

287   Gudmundsson, D. Wolf, The lithosphere-asthenosphere boundary in the North-West

288   Atlantic region, Earth Planet. Sci. Lett. 236 (2005) 249-257.

289   21. A. Mohsen, R. Kind, S. Sobolev, M. Weber, DESERT Group, Thickness of the

290   lithosphere east of the Dead Sea Transform, Geophys. J. Int. 167 (2006) 845-852.

291   22. B. Tapley, J. Ries, S. Bettadpur, D. Chambers, M. Cheng, F. Condi, B. Gunter, Z. Kang,

292   P. Nagel, R. Pastor, T. Pekker, S. Poole, F. Wang, GGM02 – An Improved Earth Gravity

293   Field Model from GRACE, J. Geodesy 79 (2005) 467-478.

294   23. M. Al-Amri, A. Al-Amri, Configuration of the seismographic networks in Saudi Arabia,

295   Seism. Res. Lett. 70 (1999) 322-331.

296   24. F. Vernon, J. Berger, Broadband seismic characterization of the Arabian Shield: Final

297   Scientific Technical Report, Department of Energy Contract No. F 19628-95-K-0015 36

298   (1998).

299   25. A. Rodgers, D. Harris, S. Ruppert, M. Pasyanos, A. Abdallah, T. Al-Yazjeen, A. Al-

300   Gazo, A broadband seismic deployment in Jordan, Seism. Res. Lett. 74 (2003) 374-381.

301   26. A. Rodgers, P. Lewis, A. Fowler, A broadband seismic deployment in the United Arab

302   Emirates, Lawrence Livermore National Laboratory Informal Document, UCRL-ID-

303   153713 (2003).

304   27. F. Sodoudi, Lithospheric structure of the Aegean obtained from P and S receiver

305   functions, PhD Thesis, Freie Universitat Berlin 2005.

306   28. J. Ligorria, C. Ammon, Poisson's ratio variations of the crust beneath North America,

307   Seism. Res. Lett. 70 (1999) 274.

308   29. K. Al-Damegh, E. Sandvol, M. Barazangi, Crustal structure of the Arabian Plate: new

309   constraints from the analysis of teleseismic receiver functions, Earth Planet. Sci. Letts.

310   231 (2005) 177-196.

311   30. G. Randall, Efficient calculation of complete differential seismograms for laterally

312   homogeneous earth models, Geophys. J. Int. 118 (1994) 245-254.

313   31. A. Rodgers, W. Walter, R. Mellors, A. Al-Amri, Y. Zhang, Lithospheric structure of the

314   Arabian Shield and Platform from complete regional waveform modeling and surface

315   wave group velocities, Geophys. J. Int. 138 (1999) 871-878.

316   32. S. McClusky, R. Reilinger, S. Mahmoud, D. Ben Sari, A. Tealeb, GPS constraints on

317   Africa (Nubia) and Arabia plate motions, Geophys. J. Int. 155 (2003) 126-138.

318   33. W. Ludwig, J. Nafe, C. Drake, Seismic refraction, in The Sea, A.E. Maxwell (Editor),

319   Wiley-Interscience, New York 1970.

320   34. G. Laske, G. Masters, A Global Digital Map of Sediment Thickness, EOS Trans. AGU

321   78 (1997) F483.

322   35. D. Turcotte, G. Schubert, Geodynamics, Cambridge University Press, 2002.

323   36. C. Ebinger, N. Hayward, Soft plates and hot spots: Views from Afar, J. Geophys. Res.

324   101 (1996) 21859-21876.

325   37. V. Camp, M. Roobol, P. Hooper, The Arabian continental alkali basalt province, part II,

326   Evolution of Harrats Khaybar, Ithnayn, and Kura, Kingdom of Saudi Arabia, Geol. Soc.

327   Am. Bull. 103 (1991) 363-391.

328   38. D. Yuen, L. Fleitout, Thinning of the lithosphere by small-scale convective

329   destabilization, Nature 313 (1985) 125-128.

330   39. S. Hansen, S. Schwartz, A. Al-Amri, A. Rodgers, Combined Plate Motion and Density

331   Driven Flow in the Asthenosphere beneath Saudi Arabia: Evidence from Shear-Wave

332   Splitting and Seismic Anisotropy, Geology 34 (2006) 869-872.

Table and Figure Captions

334 **Table 1.** Stacked boundary depths. The latitude and longitude of each station is provided, along

335 with the Moho and LAB depths obtained from the stacked SRFs and synthetic fits. A "-"

336 indicates that the depth could not be determined for that particular station either due to either a

337 lack of data or poor signal-to-noise ratios.

338 **Figure 1**. Schematic end-member rifting models. **a** Passive rifting, where the underlying

339 asthenosphere is passively upwelled and the thinnest lithosphere is offset from the rift axis. **b**

340 Active rifting, where the lithosphere is eroded by asthenospheric flow and the thinnest

341 lithosphere is coincident with the rift axis. The direction of extension is shown by the black,

342 horizontal arrows in both cases.

343 **Figure 2.** Station Map. The four different colors of triangles indicate the four seismic networks

344 included in this study. SANDSN: blue, IRIS-PASSCAL: yellow, Jordan: red, UAE: pink. The

345 corresponding station names are also listed. The dashed black line shows the boundary between

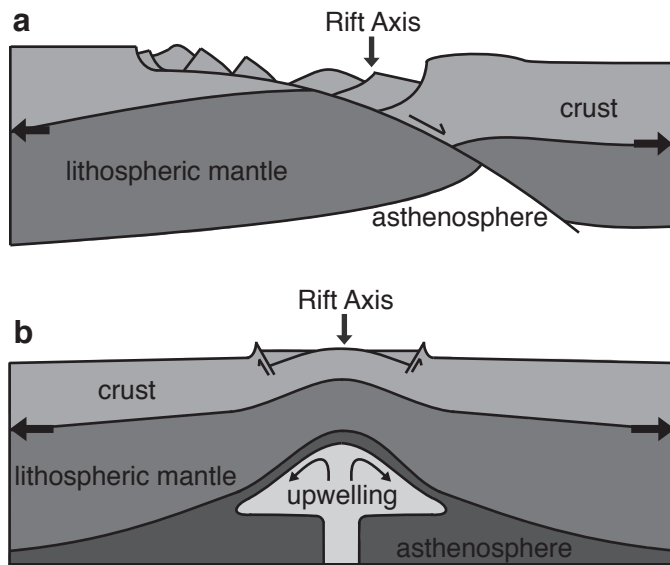346 the Arabian Shield (AS) and the Arabian Platform (AP).

347 **Figure 3.** Example SRFs. The stacked SRFs from individual stations (black) are overlain by

348 their best-fit synthetics (grey dashed lines). Station names are listed on the right. S: sediment-

349 basement boundary, M: Moho, L: LAB. **a** Gulf of Aqaba stations, **b** Red Sea coast stations, **c**

350 Arabian interior stations.

351 **Figure 4**. Maps showing the boundary depths beneath Arabia. The colored circles show the **a)**

352 Moho and **b**) LAB depths beneath individual stations where warmer colors indicate shallower

353 depths than cooler colors. The solid line marks the boundary between the Arabian Shield (AS)

354 and the Arabian Platform (AP) while the two dashed lines mark the locations of cross-sectional

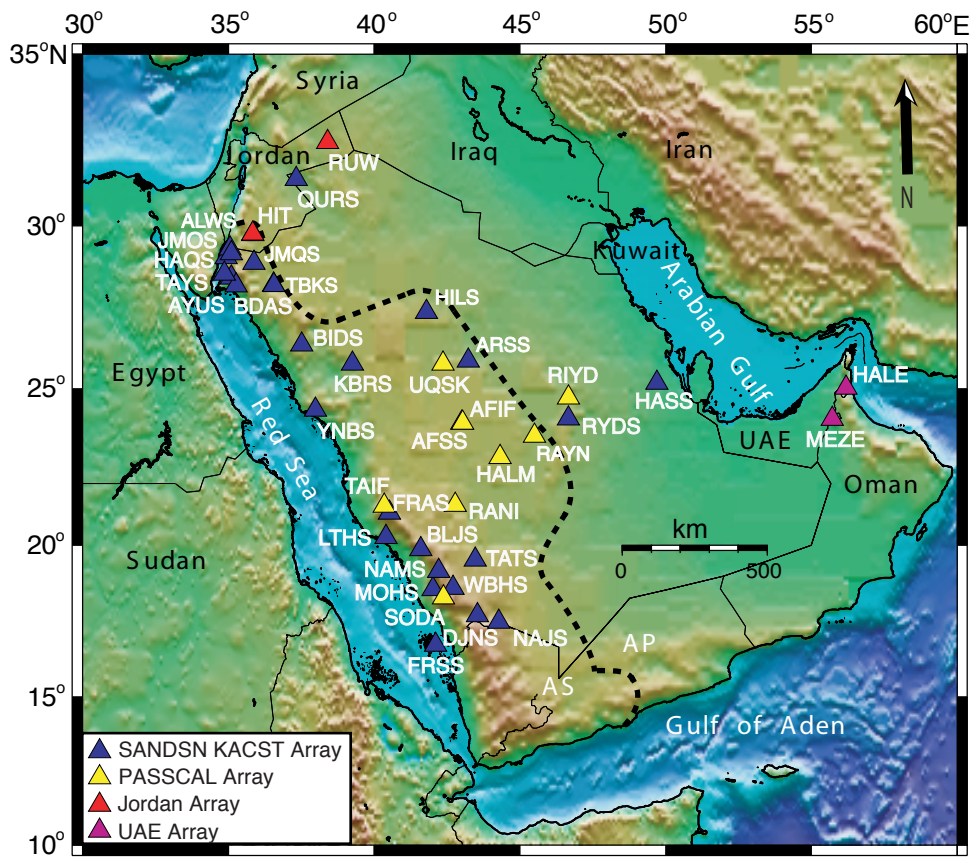355 profiles AA' and BB' in Figures 5 and 6. RS: Red Sea, GA: Gulf of Aqaba.

356   **Figure 5**. Topography, gravity signature, and lithospheric structure along cross-sectional profile

357   AA' from Figure 4. **a** Topography along the profile plotted with a 32x vertical exaggeration

358   (V.E.). The sediment thickness is shown by the grey shaded areas. **b** Comparison of the

359   observed gravity data from the GRACE satellites (black dots) and the calculated gravity (grey

360   line) resulting from the structural model shown in **c**. Red dots in **c** mark nodes that were used in

361   the gravity modeling to constrain the boundary depths, and the densities (ρ) of each layer are

362   listed. For stations along the profile, the Moho and LAB depths from the SRF analysis are

363   shown by black squares with error bars. The depth errors on the Moho and LAB were 5 and 10

364   km, respectively, and the boundary depths in the gravity model are well within the error

365   estimates.

366   **Figure 6.** Topography, gravity signature, and lithospheric structure along cross-sectional profile

367   BB' from Figure 4. **a** Topography along the profile plotted with a 16x vertical exaggeration

368   (V.E.). The sediment thickness is shown by the grey shaded areas. **b** Comparison of the

369   observed gravity data from the GRACE satellites (black dots) and the calculated gravity (grey

370   line) resulting from the structural model shown in **c**. Red dots in **c** mark nodes that were used in

371   the gravity modeling to constrain the boundary depths, and the densities (ρ) of each layer are

372   listed. For stations along the profile, the Moho and LAB depths from the SRF analysis are

373   shown by black squares with error bars. The depth errors on the Moho and LAB were 5 and 10

374   km, respectively, and the boundary depths in the gravity model are well within the error
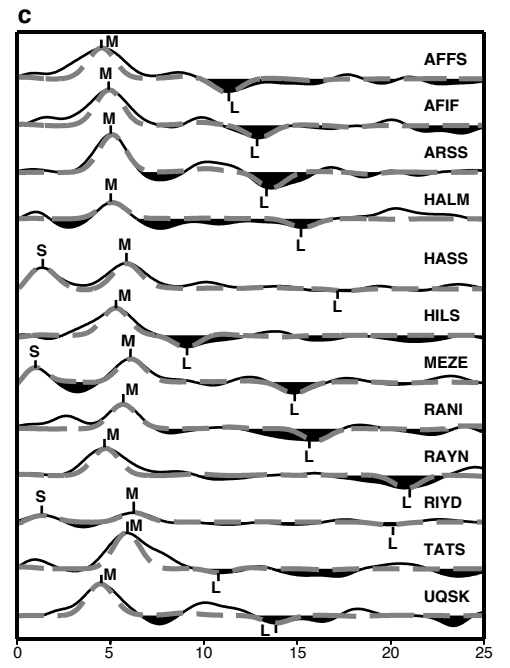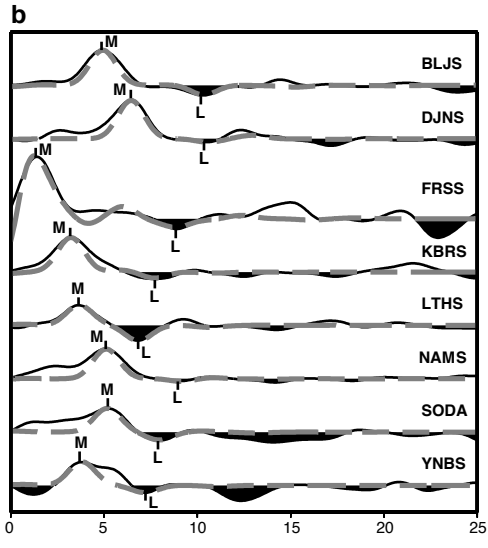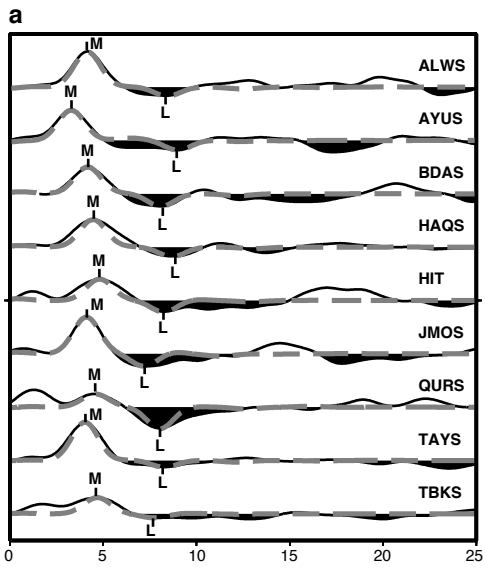
375   estimates.

Station Name	Latitude	Longitude	Moho Depth (km)	LAB Depth (km)
AFIF	23.93	43.04	35	98
AFFS	23.9267	43.0005	33	86
ALWS	29.3103	35.065	29.5	63
ARSS	25.881	43.2365	36	103
AYUS	28.1889	35.2689	24	69
BDAS	28.4317	35.1014	31	62
BIDS	26.867	36.9595	-	-
BLJS	19.8812	41.5992	35	77
DJNS	17.7073	43.5434	45	78
FRAS	21.0622	40.52	-	-
FRSS	16.7392	42.1143	12	62
HALE	25.0911	56.2394	-	-
HALM	22.8454	44.3173	38	118
HAQS	29.0548	34.9297	33	66.5
HASS	25.1899	49.6944	41.5	134
HILS	27.3835	41.7917	39	69
HIT	29.743	35.841	35.5	62.5
JMOS	29.1686	35.1094	29	54
JMQS	28.8861	35.8778	-	-
KBRS	25.7893	39.2623	23	57
LTHS	20.275	40.4107	27	52
MEZE	24.0452	55.8035	44.5	113
MOHS	18.5761	42.019	-	-
NAJS	17.5034	44.2847	-	-
NAMS	19.1714	42.2084	37.5	71
QURS	31.386	37.324	34	61
RANI	21.3116	42.7761	41.5	123
RAYN	23.522	45.5008	35	162
RIYD	24.722	46.6643	47	153
RUW	32.475	38.402	-	-
RYDS	24.19	46.64	-	-
SODA	18.2921	42.3769	38	60
TAIF	21.281	40.349	-	-
TATS	19.5412	43.4775	41.5	82.5
TAYS	28.5511	34.8717	28	61
TBKS	28.2248	36.5485	35	59
UQSK	25.789	42.36	32	106
WBHS	18.6057	42.7144	-	-
YNBS	24.3397	37.9922	28	55

a

Rift Axis

crust

lithospheric mantle

asthenosphere

b

Rift Axis

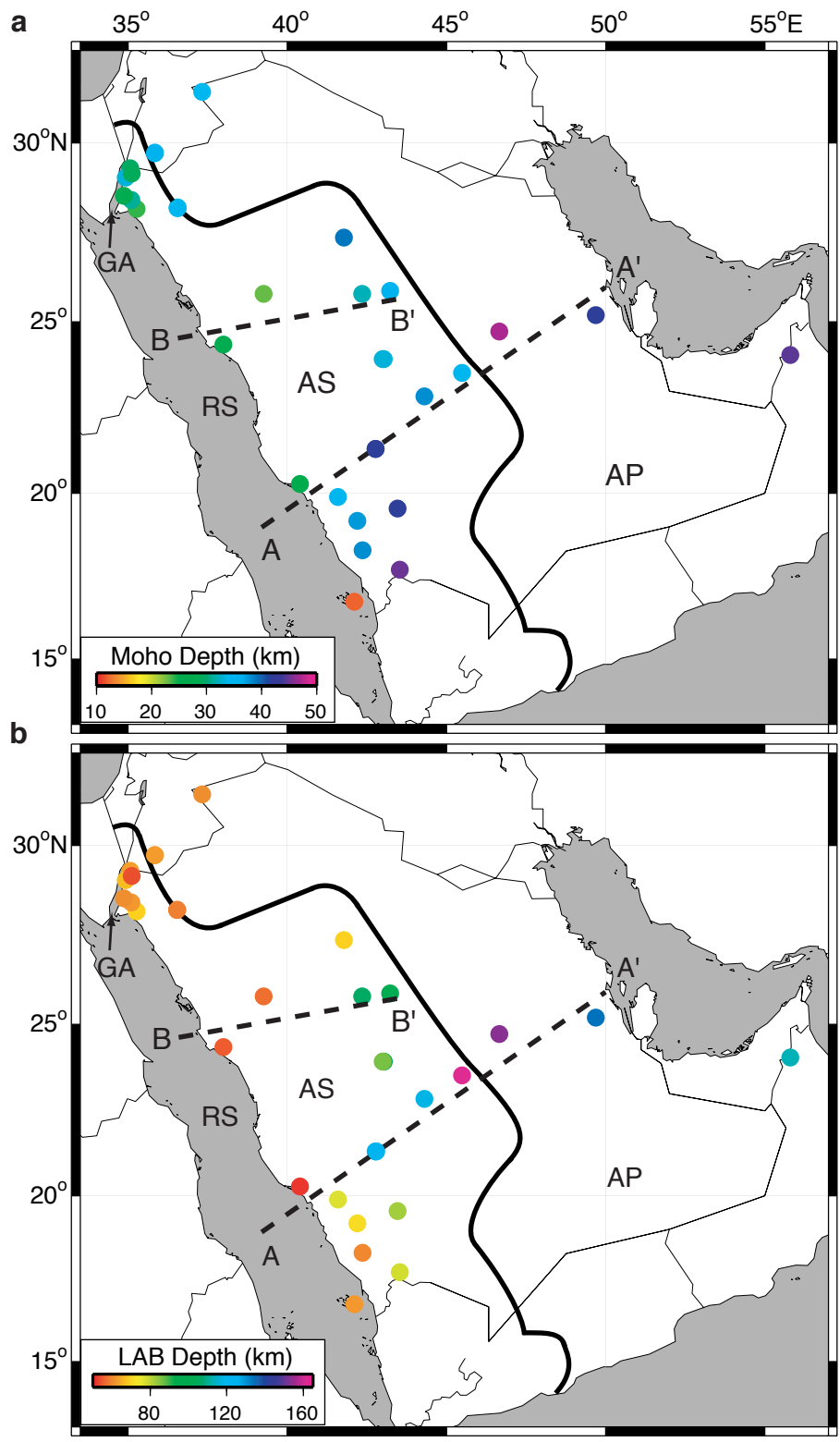crust

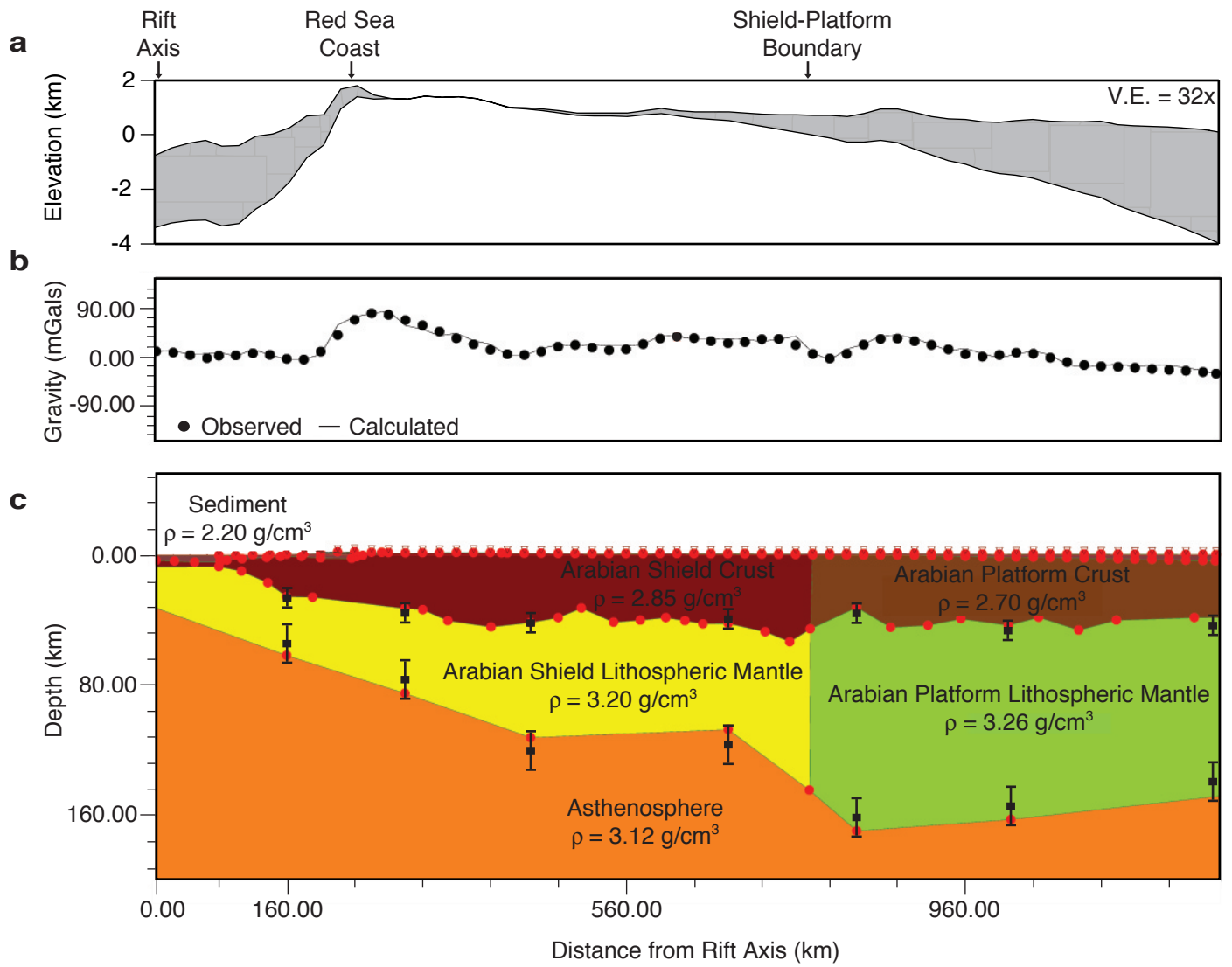lithospheric mantle

upwelling

asthenosphere

S. Hansen
Figure 1
Black-and-White
(both for print and web)

S. Hansen
Figure 2
Color
(both for print and web)
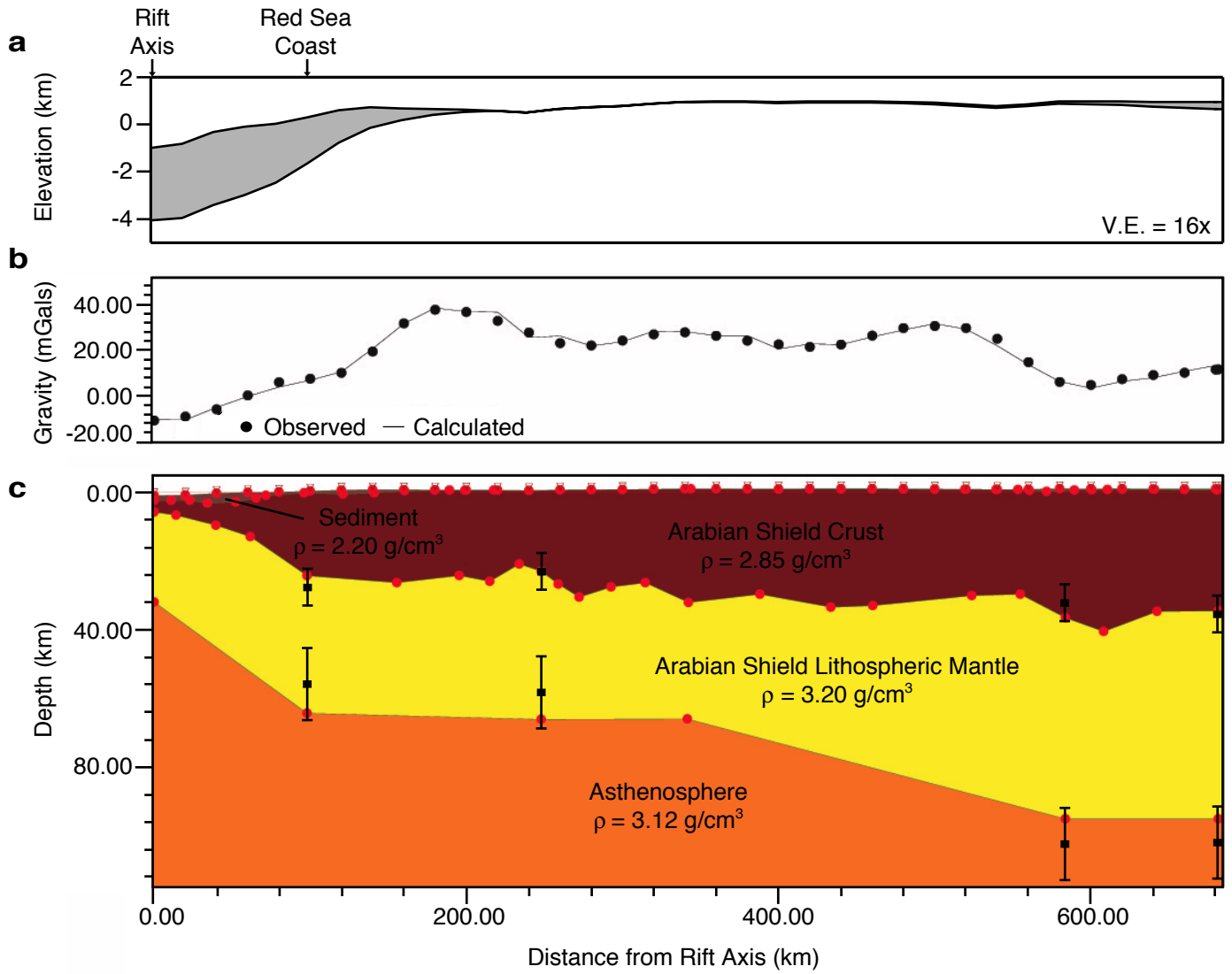
S. Hansen
Figure 4
Color
(both for print and web)

a

Rift Axis

Red Sea Coast

Shield-Platform Boundary

V.E. = 32x

Elevation (km)

b

Gravity (mGals)

90.00

0.00

-90.00

● Observed — Calculated

c

Sediment
ρ = 2.20 g/cm³

0.00

Arabian Shield Crust
ρ = 2.85 g/cm³

Arabian Platform Crust
ρ = 2.70 g/cm³

Depth (km)

80.00

Arabian Shield Lithospheric Mantle
ρ = 3.20 g/cm³

Arabian Platform Lithospheric Mantle
ρ = 3.26 g/cm³

160.00

Asthenosphere
ρ = 3.12 g/cm³

0.00   160.00   560.00   960.00

Distance from Rift Axis (km)

S. Hansen
Figure 5
Color
(both for print and web)